# Second Harmonic Generation in AlGaAs Nanowaveguides

K.A. Rutkowska[a,b,*], D. Duchesne[b], M. Volatier[c], R. Arès[c], V. Aimez[c] and R. Morandotti[b]

[a]Faculty of Physics, Warsaw University of Technology, Koszykowa 75, PL-00-662 Warsaw, Poland

[b]INRS-EMT, University of Québec, 1650 Boulevard Lionel Boulet, Varennes, Québec, J3X 1S2, Canada

[c]Centre de Recherche en Nanofabrication et en Nanocaractérisation (CRN$^2$), Université de Sherbrooke Sherbrooke, Québec, J1K 2R1, Canada

In this paper, we investigate semiconductor nanowaveguides (i.e. ridge waveguides with core-widths narrower than 1 $\mu$m) intended to act as novel optical light sources through nonlinear wavelength/frequency conversion. In particular, numerical calculations have been performed in order to design suitable photonic devices (fabricated in the AlGaAs/GaAs platform) capable of high efficiency second harmonic generation. Particular interest has been dedicated to the effective conversion of optical signals from 1520–1600 nm (the third telecom window) down to 760–800 nm. We demonstrate that the output wavelength (resulting from modal phase-matching) can be dynamically tuned by proper adjustment of the temperature and/or geometrical parameters of the waveguides. In addition, by changing the waveguide width it is also possible to modify the device dispersion characteristics, giving the possibility to work in the region of anomalous dispersion and thus allowing for the generation of temporal solitons.

PACS: 42.82.Et, 42.65.Ky, 42.79.Nv, 42.70.Mp, 78.67.Uh

## 1. Introduction

Second harmonic generation (SHG) is a second-order nonlinear optical process involving the $\chi^{(2)}$ electric susceptibility tensor. In non-centrosymmetric materials, it allows for the conversion of two pump photons into one at twice the optical frequency ($\omega + \omega \rightarrow 2\omega$) [1]. In principle, the efficiency of the SHG process relies on a phase-matching condition (derived from momentum conservation) and the interplay between the spatial beam profiles of the pump and the generated harmonic. The phase-matching condition requires the effective refractive indices of the modes at the fundamental frequency and second harmonic to be equal (as it is for type-I SHG interaction). However, this cannot be easily achieved in an arbitrary geometry due to the inherent material dispersion. For momentum conservation to be satisfied, bulk birefringent crystals (such as BBO and KTP) [2, 3] as well as waveguide geometries (in polymers [4], $LiNbO_3$ [5, 6], and semiconductors [7–11]) have been successfully used. The latter solution has recently gained a significant amount of scientific attention, resulting in the development and improvement of several phase-matching techniques in waveguiding structures. They allow for compact on-chip integration and may lead to an increased energetic efficiency (when compared to traditional bulk nonlinear crystals) [12, 13], heading thus to practical applications as integrated frequency converters for novel all-optical applications [14, 15].

Of particular importance for this paper, SHG has been previously realized in isotropic AlGaAs by way of modal phase-matching (MPM) [7, 8], quasi-phase-matching (QPM) [8–10], or artificial birefringence [8, 11]. Unfortunately, most of the proposed solutions require costly and complex fabrication procedures. In particular, they include (i) the introduction of additional thin oxidized layers of Al (in the core region of the waveguides) in order to break the isotropy of GaAs and induce artificial birefringence [11]; (ii) periodic domain orientations or quantum well intermixing [8–10] for QPM; or (iii) multi-step etching of "M-shaped" waveguides for MPM [7, 8]. In addition, even more advanced photonic structures in the form of the Bragg reflector waveguides [16], ring resonators [17], and waveguide couplers [18] suitable for SHG have also been investigated.

In this paper we propose an alternative solution based on simple AlGaAs nanowaveguides (i.e. narrow ridge waveguide structures). Their specific geometry allows for the MPM condition to be satisfied across the third telecom spectral window, as well as for a relatively high SHG efficiency due to an increased nonlinear overlap; a result of the small and tightly confined modes of this nanostructure. These devices also have numerous other advantages such as: (i) a simple fabrication process (when complex oxidization or multi-step-etching, typically required for

* corresponding author; e-mail: kasia@if.pw.edu.pl

other phase-matching techniques, are avoided); (ii) possibility of integration with other optical components on-chip (which is questionable for "M-shaped" waveguides); and (iii) tunability of the phase-matching wavelength by simply varying the temperature or through the use of various waveguides of ranging widths on a single chip. Moreover, the photonic device proposed here can be also applied for several different functionalities exploiting also the third-order nonlinearity of AlGaAs [19], such as soliton formation.

## 2. Theoretical background

Second harmonic generation can be considered as a specific case of the second-order nonlinear sum-frequency generation process (taking place in a nonlinear optical medium for which the second-order electric susceptibility $\chi^{(2)}$ is nonzero) and explained in terms of the exchange of photons between the various frequency components of the optical fields. In a quantum-mechanical description, it can be also thought of as the creation of a single photon at the frequency $2\omega$ from two input photons of fundamental frequency $\omega$.

SHG can be accomplished via a type-I interaction, whereby the second harmonic is created from a single polarized beam at the fundamental frequency, or via a type-II interaction, where two distinct beams [usually of different (e.g. linear orthogonal) polarizations] of the same fundamental frequency are used to create the second harmonic [1].

Let us consider the electric field $\tilde{E}$ of a continuous wave (CW) beams propagating in a waveguide parallel to the $z$ direction and depending on the time coordinate $t$ given by the following expression:

$$\tilde{E}_i(x,y,z) = \tilde{A}_i(z)E_i(x,y)\exp(\mathrm{i}\beta_i z - \mathrm{i}\omega_i t)\,, \qquad (1)$$

where $\tilde{A}$ is the electric field envelope, $E$ is the transverse vectorial modal electric field distribution, $\beta$ is the propagation constant, $\omega$ is the angular frequency, and the subscript $i$ refers to a specific beam.

The general evolution equations describing a type-II SHG process for a CW excitation (as defined above, i.e. achieved by neglecting the effects of chromatic dispersion, group velocity mismatch and the temporal dependence of the nonlinear response) can be obtained from Maxwell's equations by assuming a quadratic nonlinear polarization. By making use of the slowly-varying envelope approximation, and neglecting all terms not related to the SHG process (which will not be phase-matched), these evolutions equations can be written in the following form [1]:

$$\begin{cases} \partial_z A_{\mathrm{FF1}} = \mathrm{i}\eta\exp(-\mathrm{i}\Delta\beta z)A_{\mathrm{SH}}A^*_{\mathrm{FF2}} - \alpha_{\mathrm{FF1}}A_{\mathrm{FF1}}/2, \\ \partial_z A_{\mathrm{FF2}} = \mathrm{i}\eta\exp(-\mathrm{i}\Delta\beta z)A_{\mathrm{SH}}A^*_{\mathrm{FF1}} - \alpha_{\mathrm{FF2}}A_{\mathrm{FF2}}/2, \\ \partial_z A_{\mathrm{SH}} = 2\mathrm{i}\eta\exp(\mathrm{i}\Delta\beta z)A_{\mathrm{FF1}}A_{\mathrm{FF2}} - \alpha_{\mathrm{SH}}A_{\mathrm{SH}}/2, \end{cases} \qquad (2)$$

where $\partial_z$ stands for the first-order derivative with respect to the propagation direction $z$, * represents the complex conjugate, the $\alpha_i$ are the linear loss coefficients, and $\eta$ is an overlap factor [proportional to the normalized conversion efficiency described by Eq. (5)]. Please note that the electric field envelopes $A_i$ in Eq. (2) are power-normalized (thus given in units of $\mathrm{W}^{1/2}$) and differ from those introduced in Eq. (1) by

$$A = \tilde{A}\left[\left(\frac{\beta}{2\mu_0\omega}\iint |E|^2\,\mathrm{d}x\,\mathrm{d}y\right)\right]^{1/2}.$$

The phase-mismatch factor is given by $\Delta\beta = (\beta_{\mathrm{FF1}} + \beta_{\mathrm{FF2}} - \beta_{\mathrm{SH}}) = \omega(n_{\mathrm{FF1}} + n_{\mathrm{FF2}} - 2n_{\mathrm{SH}})/c$, where $n_i$ are the effective refractive indices of the $i$-th modes at a given frequency, $\omega$ is the angular fundamental frequency (FF), and $c$ is the speed of light in vacuum.

For a type-I interaction (i.e. when a single polarization state is present at fundamental frequency), Eq. (2) can be simplified to

$$\begin{cases} \partial_z A_{\mathrm{FF}} = \mathrm{i}\eta\exp(-\mathrm{i}\Delta\beta z)A_{\mathrm{SH}}A^*_{\mathrm{FF}} - \alpha_{\mathrm{FF}}A_{\mathrm{FF}}/2, \\ \partial_z A_{\mathrm{SH}} = \mathrm{i}\eta\exp(\mathrm{i}\Delta\beta z)A^2_{\mathrm{FF}} - \alpha_{\mathrm{SH}}A_{\mathrm{SH}}/2, \end{cases} \qquad (3)$$

with the phase-mismatch factor $\Delta\beta = (2\beta_{\mathrm{FF}} - \beta_{\mathrm{SH}}) = 2\omega(n_{\mathrm{FF}} - n_{\mathrm{SH}})/c$.

It can be demonstrated that the maximum conversion efficiency for type-II SHG can be obtained when the initial powers of the input pump beams are equal ($P_{\mathrm{FF1}} = P_{\mathrm{FF2}}$) [1]. Moreover, by assuming that the pump beam(s) is (are) lossless and undepleted (i.e. neglecting losses and assuming negligible depletion from the nonlinearity) the above equations [Eqs. (2), 3)] may be solved leading to the following formula describing the power of the SH signal:

$$P_{\mathrm{SH}} = \eta^2 L^2 P^2_{\mathrm{FF}}\mathrm{sinc}^2(\Delta\beta L/2)\,, \qquad (4)$$

where $L$ is the total length of propagation, and $P_{\mathrm{FF}}$ is the total power of the fundamental frequency (which is $P_{\mathrm{FF1}} + P_{\mathrm{FF2}}$ for a type-II interaction).

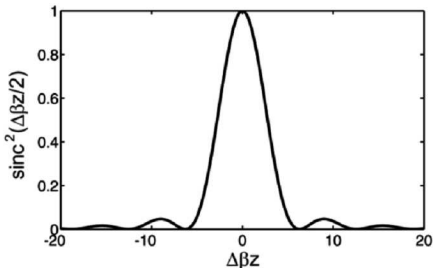


Fig. 1. $\mathrm{Sinc}^2$ function of the mismatch factor $\Delta\beta$ illustrating the dependence of the SH power in terms of the phase-matching condition.

Equation (4) predicts that the power of the generated second harmonic signal depends on the square of the input power and also decays rapidly to 0 if phase matching is not obtained. The latter is represented by a sinc squared function (see Fig. 1) which reaches 10% of its maximum value for

$$\Delta\beta z = 4.637\,, \tag{4a}$$

and thus limits the input bandwidth depending on the total distance of propagation.

When describing the efficiency of the SHG process, it is beneficial to define the normalized conversion efficiency:

$$\Gamma = \frac{P_{\mathrm{SH}}}{L^2 P_{\mathrm{FF}}^2}\,, \tag{5}$$

which is simply equal to $\eta^2$ in the case of perfect phase-matching (i.e. for $\Delta\beta = 0$) and in the absence of losses. To determine this maximal normalized conversion efficiency theoretically it is necessary to perform a vectorial analysis of the second-order nonlinear interaction, in which the full form of the susceptibility tensor is taken into consideration. The AlGaAs cubic (but non-centrosymmetric) crystal, belonging to the $\bar{4}3m$ (point) symmetry group, is characterized by the nonlinear tensor whose elements (defined with respect to the crystallographic planes) are all zero except $\chi^{(2)}_{ijk} = \chi^{(2)}$ for $i \neq j \neq k$ [1]. Here we assume that the waveguide length is parallel to the 110 crystallographic direction instead (see Fig. 2d). In the basis of the waveguide axes (defined by the Cartesian coordinates as shown in Fig. 2c), the nonlinear tensor must be rotated (by an angle of 45° in $x$–$z$ plane), resulting in the nonzero elements

$$\chi^{(2)}_{xyx} = \chi^{(2)}_{xxy} = \chi^{(2)}_{yxx} = -\chi^{(2)}_{yzz} = -\chi^{(2)}_{zzy} = -\chi^{(2)}_{zyz} \equiv \chi^{(2)}. \tag{6}$$

This results in the following form for the (nonlinear) overlap factor [13, 20]:

$$\eta = \chi^{(2)}\left(\frac{2\omega^2}{\varepsilon_0 c^3 n_{\mathrm{FF1}} n_{\mathrm{FF2}} n_{\mathrm{SH}}}\right)^{1/2} \frac{\iint_{WG} \Psi\,\mathrm{d}x\,\mathrm{d}y}{\left[\iint |E_{\mathrm{FF1}}|^2\,\mathrm{d}x\,\mathrm{d}y\right]^{1/2}\left[\iint |E_{\mathrm{FF2}}|^2\,\mathrm{d}x\,\mathrm{d}y\right]^{1/2}\left[\iint |E_{\mathrm{SH}}|^2\,\mathrm{d}x\,\mathrm{d}y\right]^{1/2}}\,, \tag{7}$$

where $\Psi \equiv E^*_{\mathrm{FF1}x}E^*_{\mathrm{FF2}x}E_{\mathrm{SH}y} + E^*_{\mathrm{FF1}x}E_{\mathrm{SH}x}E^*_{\mathrm{FF2}y} + E_{\mathrm{SH}x}E^*_{\mathrm{FF2}x}E^*_{\mathrm{FF1}y} - E^*_{\mathrm{FF1}y}E_{\mathrm{SH}z}E^*_{\mathrm{FF2}z} - E_{\mathrm{SH}y}E^*_{\mathrm{FF1}z}E^*_{FF2z} - E^*_{\mathrm{FF2}y}E^*_{\mathrm{FF1}z}E_{\mathrm{SH}z}$, $\varepsilon_0$ is the permittivity of free space, and the $x$, $y$, $z$ subscripts indicate the vectorial components of the FF1, FF2 and SH waveguide modes. As it will be discussed in the next section, a type-I interaction is forbidden in the structure analyzed here due to the particular orientation of the waveguides with respect to the AlGaAs crystallographic planes.

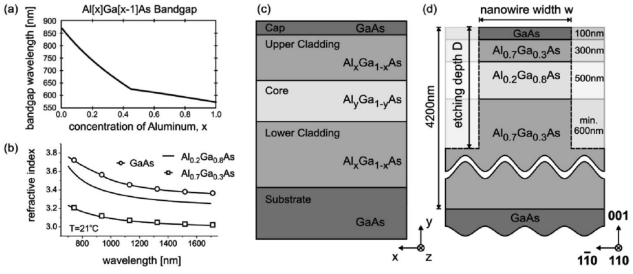


Fig. 2. Bandgap wavelength of $\mathrm{Al}_x\mathrm{Ga}_{1-x}\mathrm{As}$ as a function of the aluminum concentration (a). Material dispersion for different aluminum concentrations (b). At a fixed wavelength, a higher Al content implies a lower refractive index. An AlGaAs wafer structure (c) and the resulting post-etching nanowire geometry designed to meet the requirements for effective SHG (d). Crystallographic orientation with respect to the waveguide etched (along $z$-direction) is also presented.

It is also worth noting that the normalized efficiency $\Gamma$ is inversely proportional to the modal field area ($\Delta x \Delta y$) of the waveguide. It is thus beneficial to reduce the waveguide core size in order to enhance the confinement and thus the efficiency of the SHG process. However, reducing the core size excessively will eventually terminate the confinement, causing a significant part of the modal spatial profiles to be located in air (whose nonlinear tensor is effectively 0) and a lower overlap [13, 20].

## 3. AlGaAs/GaAs nanowaveguides

### *3.1. Device design*

AlGaAs is an ideal semiconductor for nonlinear applications, offering both a high second-order nonlinear coefficient, $\chi^{(2)} = 2d_{12} = 180$ pm/V, as well as a large third-order nonlinearity, $n_2 = 1.5 \times 10^{-17}$ m$^2$/W. Its (linear) refractive index can also be easily modified by changing the temperature or the aluminum fraction in the $\mathrm{Al}_x\mathrm{Ga}_{1-x}\mathrm{As}$ layers; see Fig. 2b [21, 22]. Moreover, the AlGaAs/GaAs structure proposed here is characterized by a mature fabrication technology, a broad infrared transparence, and allows integration with existing laser structures. The large second-order nonlinear tensor, responsible for the overall strength of the SHG process, as seen from Eqs. (4) and (7), gives rise to efficient parametric wavelength conversion [11, 23]. The established fabrication technique allows for low loss ridge waveguides with smooth sidewalls and with sub-100 nm features. Detailed information on the AlGaAs nanowaveguides fabrication process can be found in Ref. [24].

Figure 2c shows the wafer structure used for the AlGaAs/GaAs nanowaveguides design. The material refractive indices were modeled according to Ref. [21],

with suitable modifications (not applied when considering temperature dependence, as one shown in Fig. 7b) to account for absorption near the bandgap [22]. The specific compositions and thicknesses of the AlGaAs layers have been determined by requiring a strong optical confinement (obtained as a result of the high refractive index contrast between the cladding and the core layers). Moreover, by carefully choosing the aluminum content in the core layer, the bandgap of the structure can be made larger than the half-wavelength energy (see Fig. 2a), thereby minimizing any possible two-photon transitions (let us note that in general, nonlinear absorption, including two-photon absorption, is destructive and lowers the efficiency of the desired nonlinear effect). Moreover, the thickness of each layer has been determined by using 1D modal semi-vectorial analysis and optimized in order to: (i) support single mode operation in the slab structure in the spectral range of interest (i.e. 1500–1600 nm for FF); (ii) minimize the evanescent field of the modes in the substrate region. The thickness of the core was also chosen in such a way that a fundamental mode was roughly circular in shape (for $w \geq 400$ nm), an important requirement for coupling light into the device as most free space laser beams have a similar shape. Subsequently, the full-vectorial modal simulations, performed using the finite element method, allowed for the control over the remaining geometrical parameters, including the etching depth ($D$) and the width ($w$) of the designed nanowaveguides. The discretization mesh applied in the numerical algorithm has been chosen in such a way that the propagation constants were affected by a relative error smaller than 0.05%, which is well below fabrication tolerances. The simulations have allowed us to determine that a minimum etching depth of 1.5 $\mu$m is required (see waveguide cross-section presented in Fig. 2d) to prevent light leakage into the substrate. The effective refractive indices of the propagating modes and the spatial distribution of all the components of the electric and magnetic fields have been also determined through these simulations (for each waveguide width). An analysis was then performed to find possible phase matching frequencies for SHG [relating the propagation constants of FF and SH in such a way that $\Delta\beta = \beta_{\mathrm{FF1}} + \beta_{\mathrm{FF2}} - \beta_{\mathrm{SH}} = 0$ (which is simply $\Delta\beta = 2\beta_{\mathrm{FF}} - \beta_{\mathrm{SH}} = 0$ for type-I SHG)].

Moreover, it is worth to note that these photonic nanowaveguides can also be exploited for third-order nonlinear applications. This has already been shown in similar structures (as those presented in Fig. 2) where energetic requirements for nonlinear interactions were lowered [19].

Emphasis in our design was also placed to maximize the confinement and to engineer the dispersion relation [25], which is dominated by the geometric structure of the proposed nanowaveguides. Figure 3 shows the tunability of the dispersion relation for the fundamental $\mathrm{TE}_{00}$ mode as a function of the nanowaveguide width (black curves). In the same figure, the dispersion characteristics for the $\mathrm{TM}_{00}$ mode are also shown for comparison (gray curves). As one can see, the specific

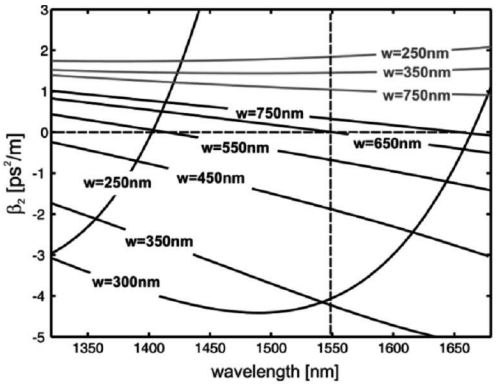


Fig. 3. Dispersion coefficient $\beta_2 = \mathrm{d}^2\beta/\mathrm{d}\omega^2$ of the AlGaAs nanowaveguide as a function of the wavelength for different core widths $w$, calculated for the $\mathrm{TE}_{00}$ (black curves) and the $\mathrm{TM}_{00}$ (gray curves) modes, respectively.

geometry and state of polarization significantly influence the total device dispersion. For the horizontally polarized first-order mode ($\mathrm{TE}_{00}$), the waveguide dispersion (resulting from the strong field confinement) becomes increasingly important as the width of the nanowaveguide is decreased and the resultant total dispersion can be inverted (with respect to the normal material dispersion at 1550 nm) and become strongly anomalous. It occurs for core widths smaller than 650 nm, at which the zero-dispersion wavelength is $\approx 1550$ nm. For the narrower structures the negative dispersion can reach significant values as low as $-4$ ps$^2$/m (for $w = 300$ nm), which is thousands of times lower than that of the typical silica fiber at 1550 nm [1]. However, a further decrease in the nanowaveguide width is not desirable, as it leads to rapid variations of the dispersion coefficient around 1550 nm (e.g. for $w = 300$ nm) or to very high normal dispersion ($\beta_2 \approx 20$ ps$^2$/m at 1550 nm for $w = 250$ nm).

Of particular importance is the anomalous dispersion regime (i.e. $\beta_2 < 0$), which can be obtained in the nanowaveguide structures due to their specific geometries. This allows the formation of temporal solitons that are generated through a balance between the anomalous dispersion and the Kerr nonlinear effect. The latter is typically inaccessible in bulk semiconductor structures or large waveguides since the material dispersion is normal and dominates. It is worth noting that the dispersion does remain normal and close to the material dispersion in the case of the vertically polarized mode ($\mathrm{TM}_{00}$), and it does not significantly change with a variation of the core width.

### *3.2. Phase-matching condition for SHG*

Based on our numerical simulations, we have found that it is possible to fulfill the modal phase-matching (MPM) condition for the fundamental wavelength in the range of 1.5–2 $\mu$m if nanowaveguides with widths of 0.3–1 $\mu$m are used. Moreover, in addition to varying the

waveguide core-size and device length, the efficiency of the nonlinear process can be controlled by several additional factors such as temperature. As discussed above, the orientation of the semiconductor wafer used for the samples plays a significant role in determining the various types of SHG processes occurring.

The effective refractive indices for the particular modes of the FF (for $\lambda = 1550$ nm, which is the central wavelength in the spectral range of interest) and the second harmonic ($\lambda = 775$ nm) as a function of the nanowaveguide width are shown in Fig. 4a. This dispersion diagram allows us to determine the MPM conditions for SHG (please note that only the fundamental modes, which are also the first-order modes, i.e. $TE_{00}$ and $TM_{00}$, at FF are considered). A type-I process corresponds to intersection points of the dispersion curves of the fundamental (black curves) and of the second harmonic frequencies (gray curves), defining the special conditions at which the effective refractive indices of the FF and SH are equal ($n_{\mathrm{FF}} = n_{\mathrm{SH}}$). On the other hand, for type-II SHG, the MPM condition is satisfied when the effective refractive index of the SH is equal to the arithmetic mean of the indices (represented by the dotted black curve in Fig. 4a) for the orthogonally polarized modes at the FF [i.e. $n_{\mathrm{SH}} = (n_{\mathrm{FF1}} + n_{\mathrm{FF2}})/2$].

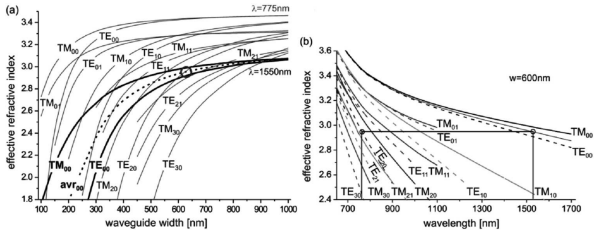


Fig. 4. Effective refractive indices obtained for the fundamental (first-order) modes of the FF (at 1550 nm — black curves) and different (first- and higher-order) modes of the SH (a). The circled areas correspond to phase-matched conditions (for type-II SHG) at which the nonlinear interaction (overlap) is particularly significant. The dispersion diagram with higher order modes for a waveguide width of 600 nm is shown in part (b). A possible mode combination supporting modal-phase matching for SHG is indicated.

It is important to note that phase matching is a necessary but not sufficient condition for the generation of efficient SH signal. Indeed, not all the possible phase matched modal combinations shown in Fig. 4a are suitable for the SHG. Additionally, the involved modes must have a significant nonlinear modal overlap. The latter depends strictly on: (i) the form of the second-order nonlinear susceptibility tensor $\chi^{(2)}$ [whose elements are determined by the symmetry properties of the optical medium and can be calculated for a fixed geometry (i.e. for fixed propagation and polarization directions)]; (ii) the spatial geometrical overlap between the particular components of the electric field of the interacting modes [1], i.e. Eq. (7).

To specifically show this result, let us focus our attention on a waveguide width of 600 nm. It has been confirmed that the lower-order mode supporting efficient SHG in this structure (in the spectral range of interest) is the $x$-polarized third-order mode ($TE_{20}$). We can thus obtain a type-II MPM condition at the fundamental wavelength of 1527.15 nm (corresponding to 763.575 nm at the SH), as can be observed from Fig. 5a (where a type-I interaction is also presented but will be shown to be forbidden due to a vanishing overlap).

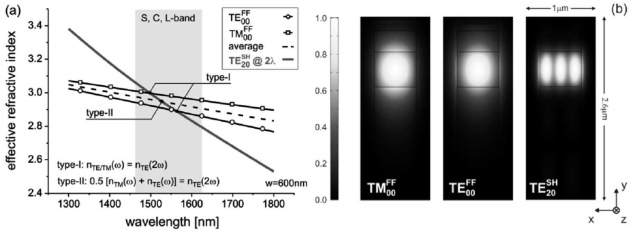


Fig. 5. Modal dispersion of the fundamental frequency (FF) modes and the third-order mode at the second harmonic (SH) for a 600 nm wide photonic nanowire, showing a type-II phase-matching wavelength at 1527.15 nm (a). The spatial distributions of the normalized electric field $(E \cdot E^*)^{1/2}$ for the modes involved in this interaction (as predicted in Fig. 5b) are shown in part (b).

While the overlap factor is given by 6 different overlap contributions [please refer to Eq. (7)], the dominant factor for the modes of interest (with the spatial profiles shown in Fig. 5b) is given by $E^*_{\mathrm{FF}1x} E^*_{\mathrm{FF}2y} E_{\mathrm{SH}x}$, which represents all major components of the involved fields. It can be easily proven that for the particular orientation of the waveguides in the AlGaAs crystallographic system analyzed here, a type-I interaction has no net efficiency for the modes under study. The main contribution to the overlap factor for this interaction (i.e. when $_{\mathrm{FF1}} =_{\mathrm{FF2}}=_{\mathrm{FF}}$ for $x, y, z$) can be written as

$$
\begin{aligned}
&\iint_{WG} E^*_{\mathrm{FF}x} E^*_{\mathrm{FF}y} E_{SHx}\,\mathrm{d}x\,\mathrm{d}y \\
&\quad = \int_D \left[ \int_{-w/2}^{w/2} E^*_{FFx} E^*_{\mathrm{FF}y} E_{\mathrm{SH}x}\,\mathrm{d}x \right] \mathrm{d}y \\
&\quad = \int_D \left[ \int_{-w/2}^{0} E^*_{\mathrm{FF}x} E^*_{FFy} E_{\mathrm{SH}x}\,\mathrm{d}x \right. \\
&\quad + \left. \int_{0}^{w/2} E^*_{\mathrm{FF}x} E^*_{\mathrm{FF}y} E_{\mathrm{SH}x}\,\mathrm{d}x \right] \mathrm{d}y \\
&\quad = \int_D \left[ \int_{0}^{w/2} E^*_{\mathrm{FF}x}(-x) E^*_{FFy}(-x) E_{\mathrm{SH}x}(-x)\,\mathrm{d}x \right. \\
&\quad + \left. \int_{0}^{w/2} E^*_{FFx}(x) E^*_{\mathrm{FF}y}(x) E_{\mathrm{SH}x}(x)\,\mathrm{d}x \right] \mathrm{d}y
\end{aligned}
$$

$$= \int_D \Bigg[ - \int_0^{w/2} E^*_{\mathrm{FF}x}(x) E^*_{FFy}(x) E_{\mathrm{SH}x}(x)\,\mathrm{d}x + \int_0^{w/2} E^*_{FFx}(x) E^*_{\mathrm{FF}y}(x) E_{\mathrm{SH}x}(x)\,\mathrm{d}x \Bigg] \mathrm{d}y = 0\,, \quad (9)$$

which is zero due to the mixing of two symmetric (with respect to $x$) [i.e. $E_{\mathrm{SH}x}(-x) = E_{\mathrm{SH}x}(x)$ and $E_{\mathrm{FF}x/y}(-x) = E_{\mathrm{FF}x/y}(x)$] and one antisymmetric [i.e. $E_{\mathrm{FF}y/x}(-x) = -E_{\mathrm{FF}y/x}(x)$] components of the modal fields in the integral.

This implies that efficient type-I interaction is forbidden for the modes considered in the waveguide geometry presented in Fig. 5b; as a result of the specific form of the nonlinear susceptibility tensor. Type-I SHG could be possible if the waveguides are etched along the crystallographic axis. For such an orientation, the nonlinear interaction overlap is proportional to $\int E_{\mathrm{FF}i} E_{\mathrm{SH}j} E_{\mathrm{FF}k}\,\mathrm{d}x\,\mathrm{d}y$ for $i \neq j \neq k$, allowing thus for an efficient nonlinear wavelength conversion taking place for the interaction resulting in the modes with the orthogonal polarization (with the preference given to $\mathrm{TM}^{\mathrm{FF}} \rightarrow \mathrm{TE}^{\mathrm{SH}}$ interactions). Please note that by assuming the first-order modes at the FF, only the odd-order (with respect to $x$-axis) SH modes (i.e. with even subscript $x$ in $\mathrm{TE}_{xy}$) are suitable due to symmetry considerations (see table in Fig. 6d).

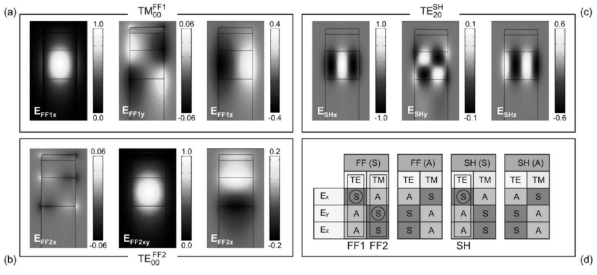


Fig. 6. Spatial distributions of the electric field components for first-order (i.e. fundamental) $\mathrm{TE}_{00}$ and $\mathrm{TM}_{00}$ modes at the fundamental frequency (for $\lambda = 1527.15$ nm) (a)–(b) and for the horizontally-polarized third-order mode at the SH (c). The table shown in part (d) is useful while performing symmetry considerations in order to find the non-vanishing overlap integrals.

Similar considerations can be performed for different combinations of the FF and SH modes, allowing one to determine all non-vanishing nonlinear interactions. A table analyzing the symmetry (with respect to the vertical axis passing through the center of the core) of the spatial profiles of the electric fields for different modes (of odd- and even-order) is shown in Fig. 6d. In particular, the spatial distributions for all the components of the transverse modal electric field for a type-II interaction considered here, i.e. $\mathrm{TM}^{\mathrm{FF}}_{00} + \mathrm{TE}^{\mathrm{FF}}_{00} \rightarrow \mathrm{TE}^{\mathrm{SH}}_{20}$ (in each case normalized to the maximum value of the major component), are shown in Fig. 6a–c. In this case, for a device length of 1 mm (typically on-chip lengths are on the order of a few millimeters at most), the acceptance bandwidth was numerically found [in accordance with Eq. (4a)] to take a value of 0.9 nm. Moreover, the maximum normalized efficiency was estimated to be approximately $950\%/\mathrm{W/cm}^2$. It is comparable to the results obtained for QPM and other MPM (e.g. "M-shaped") waveguiding devices [8], while avoiding complicated fabrication procedures. However, the normalized efficiency is less than what is found in artificially induced birefringence structures, for which (theoretical) conversion efficiencies as high as $20\,000\%/\mathrm{W/cm}^2$ have been reported [11]. The latter is primarily a result of matching the first-order modes at both fundamental and second harmonic frequencies. Nevertheless, our device still provides an appreciable efficiency while not requiring a complex oxidation process, thus lowering fabrication costs and providing a higher order of integrability with existing photonic components.

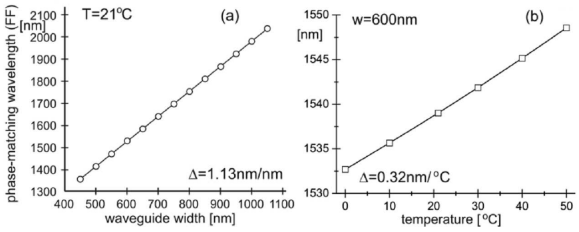


Fig. 7. Phase matching wavelength as a function of the waveguide width (a) and temperature (b).

The phase-matching relation for the type-II interaction considered above has also been studied for different waveguide widths (Fig. 7a) and varying temperature (Fig. 7b). Simulations have demonstrated that the phase-matching wavelength can be easily tuned by: (i) 1.13 nm per 1 nm of waveguide width variation (at room temperature) and (ii) 0.32 nm for each 1 °C (for a waveguide width of 600 nm), respectively.

## 4. Conclusions

In conclusion, a compact AlGaAs frequency converter based on modal-phase-matched second harmonic generation has been designed. It has been shown that the phase-matching condition can be effectively tuned either by varying the temperature or by changing the waveguide width. It is important to note that the proposed photonic structure can be achieved in practice by using low-cost and mature fabrication techniques [24]. Contrarily to other phase-matching schemes typically applied in waveguide structures, our proposed device does not require selective oxidization, multiple etching or complex wafer bonding. Moreover, a relatively high efficiency for SHG is predicted, allowing our device to be used in diverse applications, including the realization of coherent sources in otherwise unattainable spectral regions [14], and all-optical signal processing [12]. Experimental results on modal phase-matched SHG in AlGaAs nanowaveguides,

achieved using CW light source operating at the telecom wavelengths, have been reported in Ref. [26].

## Acknowledgments

K. Rutkowska would like to acknowledge the Marie Curie Outgoing International Fellowship (MOIF-CF--2006-039600). This work was also supported by the FQRNT (Fonds Québécois de la Recherche sur la Nature et les Technologies), the NSERC (Natural Sciences and Engineering Research Council of Canada), and the INRS (Institut national de la recherche scientifique).

## References

[1] R.W. Boyd, *Nonlinear Optics*, Academic Press, New York 2008.

[2] A. Fiore, M. Photographic, E. Rosencher, R. Soria, J. Nagle, *Nature* **391**, 463 (1998).

[3] H. Kim, L. Jankovic, G. Stegeman, S. Carrasco, L. Torner, M. Katz, D. Eger, *Acta Phys. Pol. A* **103**, 107 (2002).

[4] T.C. Kowalczyk, K.D. Singer, P.A. Cahill, *Opt. Lett.* **15**, 2273 (1995).

[5] K.R. Parameswaran, R.K. Route, J.R. Kurz, R.V. Roussev, M.M. Fejer, M. Fujimura, *Opt. Lett.* **27**, 179 (2002).

[6] G. Du, G. Li, S. Zhao, W. Qiao, K. Yang, J. An, M. Li, J. Wang, W. Wang, *Acta Phys. Pol. A* **115**, 685 (2009).

[7] S. Ducci, L. Lanco, V. Berger, A. De Rossi, V. Ortiz, M. Calligaro, *Appl. Phys. Lett.* **84**, 2974 (2004).

[8] S. Venugopal Rao, K. Moutzouris, M. Ebrahimzadeh, *J. Opt. A, Pure Appl. Opt.* **6**, 569 (2004).

[9] X. Yu, , L. Scaccabarozzi, J.S. Harris, Jr., P.S. Kuo, M.M. Fejer, *Opt. Expr.* **13**, 10742 (2005).

[10] M.M. Fejer, G.A. Magel, D.H. Jundt, R.L. Byer, *IEEE J. Quant. Electr.* **28**, 2631 (1992).

[11] L. Scaccabarozzi, M.M. Fejer, Y. Huo, S. Fan, X. Yu, J.S. Harris, *Opt. Lett.* **31**, 3626 (2006).

[12] C. Langrock, , S. Kumar, J.E. McGeehan, A.E. Willner, M.M. Fejer, *J. Lightw. Technol.* **24**, 2579 (2006).

[13] A.M. Zheltikov, *Opt. Commun.* **270**, 402 (2007).

[14] M.M. Fejer, *Phys. Today* **47**, 25 (1994).

[15] A. Arie, K. Fradkin-Kashi, Y. Shreberk, *Opt. Lasers Eng.* **37**, 159 (2002).

[16] P. Abolghasem, J. Han, B.J. Bijlani, A. Arjmand, A.S. Helmy, *IEEE Photon. Technol. Lett.* **21**, 1462 (2009).

[17] Z. Yang, P. Chak, A.D. Bristow, H.M. van Driel, R. Iyer, J.S. Aitchison, A.L. Smirl, J.E. Sipe, *Opt. Lett.* **32**, 826 (2007).

[18] P. Dong, J. Upham, A. Jugessur, A.G. Kirk, *Opt. Expr.* **14**, 2256 (2006).

[19] G.A. Siviloglou, S. Suntsov, R. El-Ganainy, R. Iwanow, G.I. Stegeman, D.N. Christodoulides, R. Morandotti, D. Modotto, A. Locatelli, C. De Angelis, F. Pozzi, C.R. Stanley, M. Sorel, *Opt. Expr.* **14**, 9377 (2006).

[20] H. Ishikawa, T. Kondo, *Appl. Phys. Expr.* **2**, 042202 (2009).

[21] S. Gehrsitz, F.K. Reinhart, C. Gourgon, N. Herres, A. Vonlanthen, H. Sigga, *J. Appl. Phys.* **87**, 7825 (2000).

[22] S. Zollner, *J. Appl. Phys.* **90**, 515 (2001).

[23] M. Bhashi, T. Kondo, R. Ito, S. Fukatsu, Y. Shiraki, K. Kumata, S.S. Kano, *J. Appl. Phys.* **74**, 596 (1993).

[24] M. Volatier, , D. Duchesne, R. Morandotti, R. Arès, V. Aimez, *Nanotechnol.* **21**, 134014 (2010).

[25] J. Meier, W.S. Mohammed, A. Jugessur, L. Qian, M. Mojahedi, J.S. Aitchison, *Opt. Expr.* **15**, 12755 (2007).

[26] D. Duchesne, K.A. Rutkowska, M. Volatier, F. Légaré, S. Delprat, M. Chaker, D. Modotto, A. Locatelli, C. De Angelis, M. Sorel, D.N. Christodoulides, G. Salamo, R. Ares, V. Aimez, R. Morandotti, *Opt. Expr.* **19**, 12408 (2011).